J Mater Sci (2025) 60:22159–22173

Electronic materials

Tuning optoelectronic properties of $CsPbI_2Br$ perovskite films via octadecyl ammonium iodide substitution

Sandile Thubane[1], Nolwazi Nombona[2], and Mmantsae Diale[1,*]

[1] *Present Address: Department of Physics, University of Pretoria, Private Bag X20, Hatfield, Pretoria 0028, South Africa*
[2] *Department of Chemistry, University of Pretoria, Private Bag X20, Hatfield, Pretoria 0028, South Africa*

Received: 5 August 2025
Accepted: 7 October 2025
Published online: 24 October 2025

ABSTRACT

Metal halide perovskites such as $CsPbI_2Br$ are promising candidates for next-generation optoelectronic devices due to their tuneable bandgaps, high light absorption, and solution processibility. However, their practical application is hindered by structural purity, high defect densities, and non-radiative carrier losses, all of which limit efficiency and long-term stability. Recent strategies to mitigate these challenges involve compositional engineering with bulky organic cations and careful control of post-deposition annealing, but the combined influence of thermal processing and partial organic substitution on $CsPbI_2Br$ remains insufficiently understood. In this work, we report the synergistic impact of thermal annealing and partial organic cation substitution on the structural, morphological, and optoelectrical properties of $CsPbI_2Br$ perovskite thin films. Varying the annealing temperature and the substitution of Cs^+ with octadecyl ammonium iodide (ODAI) can tune the crystallinity, defect density, and carrier recombination properties. X-ray diffraction analysis revealed a tetragonal crystal structure with optimal crystallinity at 240 ℃ and signs of phase transition at 300 ℃. Field emission scanning electron microscopy images confirm enhanced grain size and uniformity upon substitution with 15 mol% ODAI. The films with low ODAI concentration ($ODA_{0.15}$) exhibit reduced micro strain and dislocation density, maintaining structural integrity while passivating defects. Ultraviolet–visible absorption spectra show bandgap narrowing with moderate substitution, while photoluminescence measurements demonstrate significantly enhanced emission intensity in $ODA_{0.15}$ film, indicating suppressed non-radiative recombination. Excessive ODAI ($ODA_{0.25}$ or higher) leads to lattice distortion, phase inhomogeneity, and reduced optical performance. These results highlight the importance of precise ODAI control and annealing conditions for optimizing $CsPbI_2Br$ perovskites, providing a viable route toward efficient and stable optoelectronic devices.

Handling Editor: Kevin Jones.

Address correspondence to E-mail: mmantsae.diale@up.ac.za

https://doi.org/10.1007/s10853-025-11654-3

Introduction

All-inorganic perovskites have emerged as promising materials for solar cells, and light-emitting diodes owing to their superior thermal stability, and excellent optoelectronic properties such as high absorption coefficient [1], long charge-carrier diffusion lengths [2], and tuneable bandgap [3]. $CsPbI_2Br$ perovskite possess a suitable bandgap (~ 1.9–2.0 eV) [4] and enhanced environmental stability compared to its organic–inorganic counterparts. However, its practical application is hindered by issues such as poor film morphology [5], phase instability under thermal stress [6], and high defect densities [7] that contribute to non-radiative recombination ultimately reducing device performance.

Several approaches have been explored to overcome these limitations, including surface passivation [8], optimization of growth techniques [9], and compositional engineering [10]. In a study done by Chen et al., it was revealed that a fluorinated organic ammonium halide salt used as a surface passivator in $CsPbI_2Br$ perovskite can significantly reduce trap densities by filling the pinholes and gaps between the grains [8]. In another study, Fan et al., optimized the deposition speed for the fabrication of highly crystalline, uniform, and pinhole-free $CsPbI_2Br$ perovskite films using a blade coating technique. Their results revealed that a well-controlled film formation via leveraging processing temperature could effectively counterbalance negative influences from moisture attack yielding uniform and pin-hole free films [9]. Ozturk et al., advocated that a small amount of $FeCl_2$ can effectively reduce defect states in $CsPbI_2Br$ perovskite [10]. Among these, thermal annealing also plays a critical role in facilitating crystallization, grain growth, and defect passivation in perovskite materials. Precise thermal annealing can significantly improve film quality and optoelectronic properties, while over-heating can induce phase segregation or lead to structural degradation [11].

Another promising strategy involves the incorporation of bulky organic cations which can partially occupy the A-site within the perovskite lattice or accumulate at the grain boundaries to passivate defects. Previous studies have demonstrated that such alkylammonium additives can enhance moisture resistance, suppress defect states, and improve film morphology. However, excessive incorporation may disrupt the 3D perovskite lattice, leading to insulating layers or phase separation. Wu et al., incorporated ethyl ammonium into a methylammonim-based perovskite and deduced that a bulky organic cation can cause lattice strain through lattice contraction or dilation in addition to phase transitions by octahedral tilting [12].

In this work, we systematically investigate the effects of thermal annealing and octadecyl ammonium iodide (ODAI) substitution on the structural, morphological, and optoelectronic properties of $CsPbI_2Br$ perovskite films. Crystallinity, micro strain, dislocation density, grain size, and optical properties were evaluated using X-ray diffractometer (XRD), scanning electron microscopy (SEM), Ultraviolet–visible (UV–vis) spectroscopy, and photoluminescence (PL) analysis. Our results show that moderate ODAI incorporation ($ODA_{0.15}$) coupled with optimized annealing (240–280℃) significantly enhances film quality and photophysical performance, while excessive substitution or annealing degrades the resulting material. These insights provide valuable guidelines for processing high-quality, stable $CsPbI_2Br$ films for future optoelectronic device applications.

Experimental

Materials

Glass/Fluorine-doped tin-oxide (FTO) substrates with a thickness of 2.2 mm, and resistivity of ~ 7 Ω/sq were used for all film depositions and characterizations. Caesium iodide (CsI: 99.9%), lead bromide ($PbBr_2$: 98.0%), octadecyl amine (ODA: 99.0%), dimethylformamide (DMF: 99.8%), dimethyl sulfoxide (DMSO: 99.9%), acetone (Ch_3COCH_3: 58.1%), isopropanol ($CH_3CHOHCH_3$: 60.1%), and hydroiodic acid (HI: 57 wt% in water) were purchased from Sigma Aldrich. All the materials were used as received without any further purification.

Preparation of precursors and thin films

Octadecyl ammonium iodide was synthesized by placing 10 g of octadecyl amine in an ice-bath flask, then 10 mL of hydroiodic acid was added while stirring the solution for 3 h to complete the reaction. The mixture was cooled to room temperature and then transferred

to an oil-bath heating plate at 90 ℃ with stirring until the solution became dry. The raw product was washed with diethyl ether three times followed by drying and recrystallization in an oven at 60℃ overnight.

A mixture of (1:4) DMSO:DMF was used to improve the solubility of Br^- in $PbBr_2$ precursor. The perovskite precursors were synthesized by reacting 208 g CsI, 184 g PbI_2, and 148 g $PbBr_2$ in 1 mL of DMSO:DMF solution. The solution was stirred for 6 h on a hot plate at 90 ℃ to achieve solution homogeneity. Partial substitution of Cs^+ with a long-chain ODA^+ was performed to synthesise a mixed A-site $ODA_xCs_{1-x}PbI_2Br$ perovskite. Prior the deposition of the perovskite films, the substrates were subjected to a cleaning procedure to ensure surface uniformity and validity of the findings for optimal perovskite film growth. The procedure involves sonication in acetone, isopropanol, and deionized water sequentially for 15 min, then dried with nitrogen-stream. UV-ozone treatment was done for 15 min to remove organic contaminants and induce surface wettability. The one-step spin coating method shown in Fig. 1 demonstrates both pristine and partially substituted perovskite film growth, where 60 µL of the precursor was spin-coated on a preheated (75 ℃) 1 × 1 mm FTO substrate at a speed of 2000 rpm for 30 s. Subsequently the films were annealed at 200–300 ℃ to achieve optimal crystallinity and phase purity.

Characterizations

Structural properties of the perovskite thin films were investigated using Bruker D2-Phaser X-ray diffractometer (XRD) with Cu Kα radiation of a wavelength of 0.15405 nm. The XRD was fitted with a copper X-ray tube operating at 40 mA and 45 kV. The measurements were acquired in the 2θ range 5–40° in steps of 0.05°. Structural phase, crystallinity, and crystallite size were extracted from the diffractograms. Field Emission Scanning Electron Microscopy (FE-SEM, Zeiss 55 Utra, Germany) was used to study the morphology of the perovskite films at an accelerated voltage of 2 kV using an inlense detector in high vacuum environment at room temperature. ImageJ software was used to determine the diameter of the particles. Optical absorption spectra were measured using an Agilent Cary 60 ultra-violet visible (UV–Vis) spectrophotometer with a wavelength of incident light ranging from 400–800 nm. The UV–Vis instrument was equipped with a double-beam system made up of a xenon flash lamp light source. A standard reference material was used for calibration and baseline correction to ensure precise characterisation and account for substrate contributions. Photoluminescence (PL) emissions were examined using a confocal microscope (Ti-E Motorized inverted Microscope, Nikon) with a single-photon avalanche diode (Excelitas Technologies SPCM-AQRH-TR) and an Electron Multiplying CCD camera (Andor iXon 3 897 DU-897E-CS0-EXF). The excitation was carried out using a supercontinuum pulsed laser (SuperK EVO, NKT Photonics) with a pulse width of ≈67 ps and an average power of ≈359 ± 6 nW operating

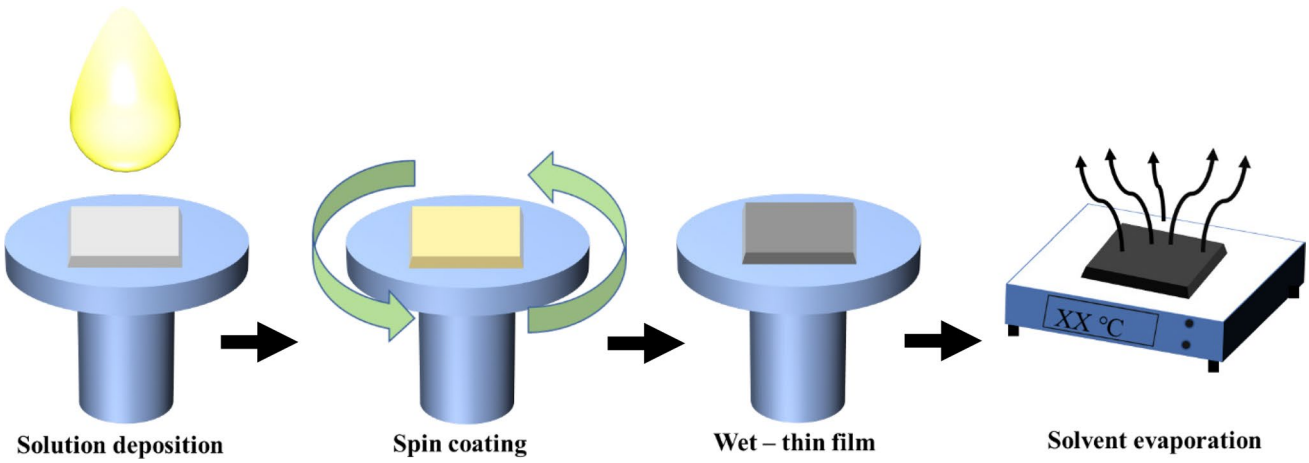

Figure 1 Solution processing of $ODA_xCs_{1-x}PbI_2Br$ perovskite thin films.

at 20 MHz repetition rate where the excitation light was filtered to 590 nm wavelength (SuperK VARIA, NKT Photonics, 10 nm bandwidth).

Results and discussion

Structural properties

XRD patterns of $CsPbI_2Br$ perovskite thin films fabricated via a one-step solution deposition method and annealed at temperatures ranging from 200 to 300 ℃ are shown in Fig. 2a. The peaks observed at 2θ: 14.8°, 21.0°, 24.6°, 29.7°, 33.8° and 37.8° are a hallmark of a photoactive tetragonal $CsPbI_2Br$ perovskite structure. In addition, the peak positions closely agree with previously observed values for $CsPbI_2Br$ perovskite [6]. Prominent diffraction peaks observed at 2θ: 14.8° and 29.7° were assigned to the (100) and (200) phase, respectively. Moreover, the minor peaks located at 21.0°, 24.6°, 33.8°, and 37.8° correspond to the (110), (111), (210), and (211) planes, respectively as proposed by Zheng et al. [6].

At low temperatures of 200–220 ℃, the peaks are relatively broad and are less intense indicating smaller crystallite sizes and possibly incomplete crystallization. The peaks become more intense and narrower at moderate temperature (240–260 ℃), suggesting enhanced crystallinity. Maximum peak intensity is reached at higher temperatures (280–300 ℃) indicating best crystallinity. The increasing intensity of the peaks may also suggest improved orientation and possible grain growth. Crystal structure of perovskite materials is influenced by the annealing temperature resulting in the formation of secondary phases and excessive annealing beyond optimal temperature may lead

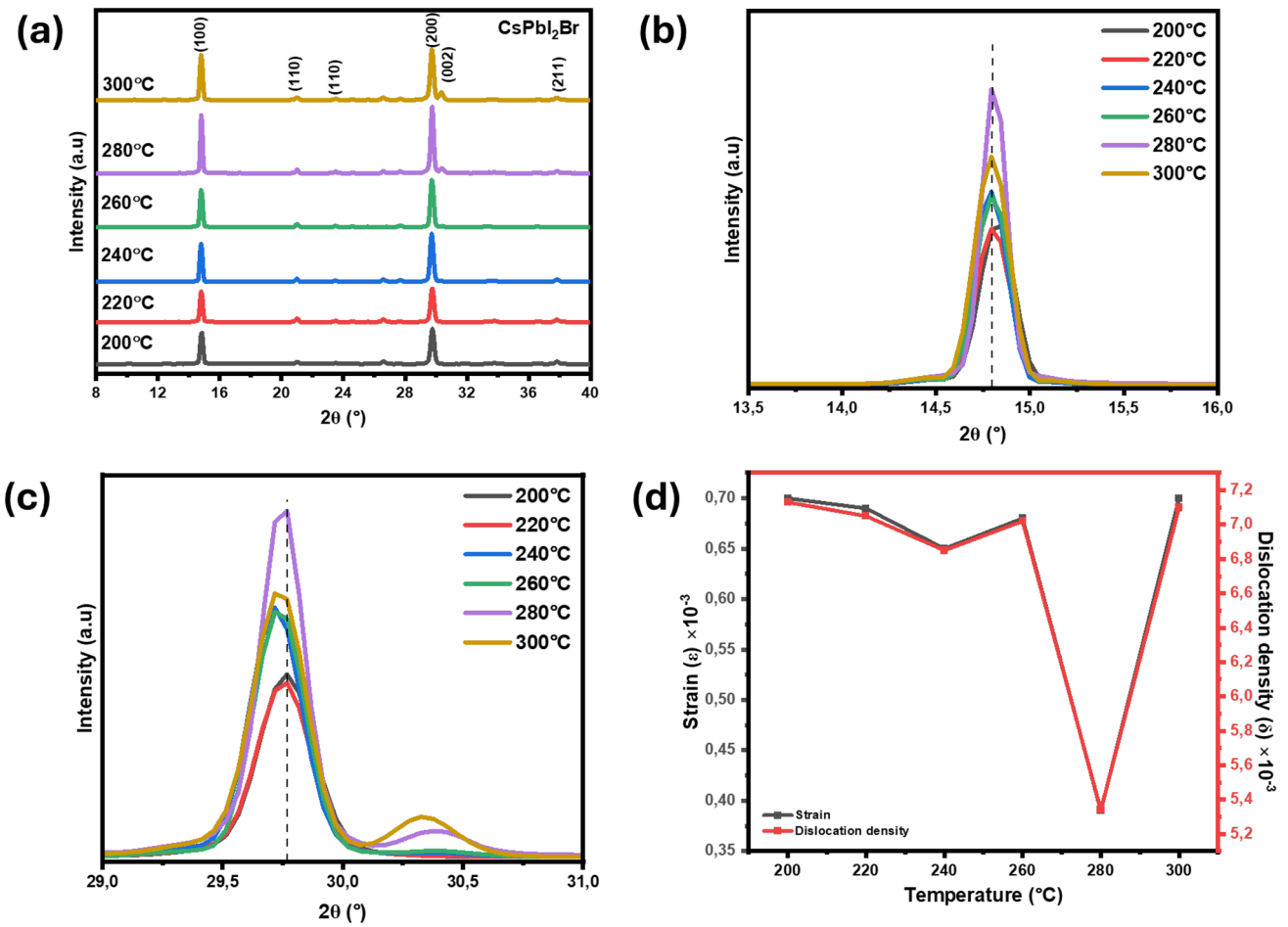

Figure 2 **a** XRD patterns of $CsPbI_2Br$ perovskite annealed at various temperatures, **b** Zoom-in of the (100) diffraction plane, **c** Zoom-in of the (200) diffraction plane, **d** variation of micro strain and dislocation as function of annealing temperature.

to the decomposition of the perovskite film. A (001) peak of the excess PbI_2 commonly appears around 12.6°, which is not clearly evident in Fig. 2a, therefore the inorganic perovskite decomposition is not dominant at high temperature. This suggests that the peak observed at 30.3° during the annealing at temperatures above 240 ℃ could be due to the formation of a new $CsPbBr_3$ perovskite phase as confirmed by the PDF#18–0364. Temperature-induced phase transition was also shown by Kong et al., using all-inorganic perovskite, where $CsPbI_3$ revealed a polymorph transition temperature of 300℃ to cubic α- phase perovskite [13]. A more detailed review of the (100) and (200) reflections is shown in Fig. 2b, c, respectively. The zoomed-in (110) and (200) peaks reveal that as the temperature increases, the diffraction peaks become sharper and more intense reaching a maximum at 280 ℃ then slightly stabilizing at 300 ℃. This may suggest bigger crystallite size and improved crystal order (geometry) during annealing at 280 ℃. Scherrer *Eq.* 1 was used to reveal contribution of crystallite size (D, nm) on the intensity of the diffraction peaks at various temperature.

$$\beta = \frac{K\lambda}{D\sin\theta} \tag{1}$$

where K is the Scherrer constant (0.9), λ is the wavelength of the x-ray source (0.154056 nm), β is the full width at half maximum (FWHM) and θ is the peak position. The FWHM is a parameter used to observe peak broadening which is related to the arrangement of crystallites in polycrystalline materials. It is a product of factors such as instrumental broadening and true crystal broadening. The true crystal broadening was extracted by simulating a Gaussian correction for the highest intensity peaks to remove broadening resulting from the instrument related by *Eq.* 2:

$$\beta^2 = \beta_{obs}^2 - \beta_{ins}^2 \tag{2}$$

were β is the intrinsic broadening of the $CsPbI_2Br$ perovskite, β_{obs} is the observed broadening acquired from the diffraction peaks, and β_{ins} is the broadening caused by the instrument. The corresponding crystallographic parameters, including FWHM, crystallite size, and calculated crystallinity for (100) and (200) diffraction planes, are summarized in Table 1.

The data suggests that as temperature increases, the intensity of the diffraction peaks enhances with the narrowing of the FWHM, indicating improved crystallinity. Notably, the highest peak intensity is observed at 280℃, suggesting optimal crystal growth. At this temperature, the films exhibited the lowest FWHM of 0.159° and 0.227° for the (100) and (200) planes, respectively, attributed to the large crystallite sizes. This suggests that annealing at 280 ℃ promotes effective grain and crystal growth. Interestingly, despite the slight decrease in crystallite size at 300 ℃, the crystallinity continues to increase, reaching a maximum of 78.59%. This may be attributed to further improvement in long-range ordering of crystallites and possibly reduced defect density despite the slight reduction in crystallite size. The improvement in long range ordering can be is further supported by the decreasing dislocation density and strain observed in Fig. 2d. Both parameters exhibit nearly overlapping decreasing trends with increasing temperature. This correlation arises as a result of strain-induced lattice distortions contributing to XRD peak broadening, while dislocation density is inversely related to crystallite size, which also depends on the same peak broadening. At 240℃ $CsPbI_2Br$ perovskite revealed less dislocation, improving the crystallite packing and reaching the low dislocation density and strain suggesting high film quality. Furthermore, at annealing of 280 ℃ the film depicts the highest peak intensity and crystallinity. At this temperature, the films possess the dominant tetragonal structure prior the formation

Table 1 Full width at half maximum and crystallite size estimated from the peaks located at 2θ: 14.8° and 29.7° including crystallinity at varying temperature

Temperature (℃)	Parameter	(100) Peak (°)	(200) Peak (°)	Crystallinity (%)
200	β (°)	0.213	0.276	69.65
	D (nm)	37.66	29.81	
220	β (°)	0.211	0.268	69.42
	D (nm)	38.17	30.63	
240	β (°)	0.204	0.257	75.84
	D (nm)	39.30	31.95	
260	β (°)	0.209	0.252	70.89
	D (nm)	38.31	32.68	
280	β (°)	0.159	0.227	73.94
	D (nm)	50.37	36.21	
300	β (°)	0.211	0.271	78.59
	D (nm)	37.91	30.33	

of a new phase. A similar phenomenon was observed by Nam et al., where they showed that a temperature of 280℃ is sufficient to fabricate high-quality $CsPbI_2Br$ perovskite [14]. Consequently, annealing reduces structural disorder and improves crystallinity, while lowering both micro strain and dislocation density. These results suggest that high annealing temperature can enhance film quality and potentially device performance as a result of improved structural properties.

This work further explores the substitution of Cs^+ using ODA^+ because of its hydrophobic nature to minimize micro strain for possible improvement in stability. Duan et al., confirmed the wetting properties of ODA^+ through contact angle measurements using $FAPbBr_3$ as the pristine film. Their results revealed that ODA-treated films had a high contact angle of 70° compared to the pristine material with a contact angle of 39° [15]. Thermal stability of ODA^+ was investigated through thermogravimetric analysis shown in Fig. 3a. The spectra show a single stage decomposition of the organic molecule. ODAI sample initially has ~ 100% weight and begins to decline from around 270–280 ℃, with a steep drop near 320–350 ℃. This suggests that ODAI remains thermally stable up to around ~ 270 ℃, exhibiting negligible mass loss. No detectable decomposition products such as iodide salts or carbonaceous residues above 400 ℃ confirming the purity of ODAI molecule. The derivative thermogravimetry peak appears near ~ 340 ℃ indicating the maximum decomposition temperature. This peak is likely associated with the

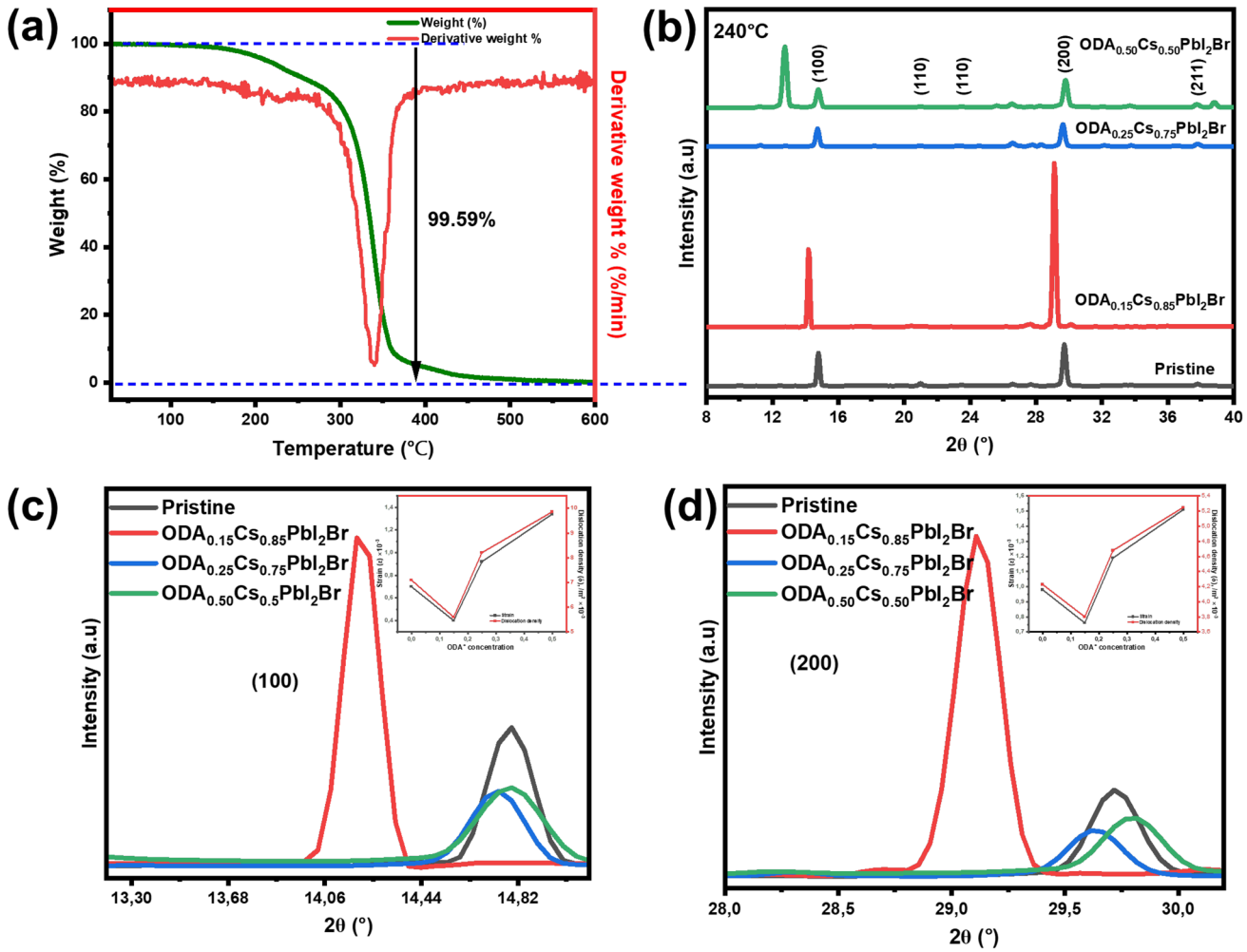

Figure 3 **a** Thermal degradation of ODAI, **b** XRD spectra of $CsPbI_2Br$ films partially substituted with ODAI and annealed at 240℃, **c** Zoomed-in view of the (100) peak with corresponding strain and dislocation density (inset), **d** Zoomed-in view of the (200) peak with corresponding strain and dislocation density (inset).

breakdown of the long alkyl chain and iodide salt decomposition.

The inability of Cs^+ to support the octahedral $[PbX_6]^{4-}$ can lead to poor stability as a resulting from low tolerance factor for $CsPbI_2Br$ [16]. Partial substitution of Cs^+ with ODA^+ was explored to unveil its effects on the $CsPbI_2Br$ perovskite crystal structure. The ODA^+ concentration was varied: $ODA_{0.15}Cs_{0.85}PbI_2Br$ ($ODA_{0.15}$), $ODA_{0.25}Cs_{0.75}PbI_2Br$ ($ODA_{0.25}$), and $ODA_{0.50}Cs_{0.50}PbI_2Br$ ($ODA_{0.50}$), annealed at 240 ℃ and XRD measurements shown in Fig. 3b were carried out. All the samples maintained characteristic reflections of the $CsPbI_2Br$ perovskite phase with no observable peaks associated with secondary phases of CsI, PbI_2, or ODAI residues, indicating successful incorporation of the organic cation without phase segregation. The diffraction patterns showed noticeable changes in peak intensity and width as ODAI concentration increases, implying a structural evolution facilitated by the introduction of the bulky organic cation. Zoomed-in views of the (100) and (200) planes in Fig. 3c and Fig. 3d, respectively, further elucidate these structural modifications. A distinct shift and broadening of peaks are observed with increasing ODAI concentration resulting in lattice shifts. Qualitative analysis in Table 2 revealed that the FWHM for the (100) plane in $ODA_{0.15}$ decreases from 0.204 to 0.160 nm upon annealing at 240 ℃, corresponding to an increase in crystallite size from 39.30 to 50.09 nm for the pristine film. Furthermore, the (200) diffraction plane follows the same trend corroborating the increase in crystallite size from 31.95 to 36.30 nm. The (100) reflection shows reduced intensity and increased FWHM, suggesting a disruption of long-range order and decreased

Table 2 Effects of partial substitution using ODA^+ on the crystal structure of $CsPbI_2Br$ at 280℃

ODA^+ concentration	Parameter	(100) Peak (°)	(200) Peak (°)	Crystallinity (%)
240℃				
Pristine	β (°)	0.204	0.257	75.84
	D (nm)	39.30	31.95	
	Strain	0.648	0.980	
	Dislocation	6.853	4.230	
$ODA_{0.15}$	β (°)	0.160	0.226	57.92
	D (nm)	50.09	36.30	
	Strain	0.399	3.327	
	Dislocation	5.597	8.386	
$ODA_{0.25}$	β (°)	0.230	0.284	71.79
	D (nm)	32.91	28.99	
	$\varepsilon \times 10^3$ (nm^{-2})	0.923	1.191	
	Dislocation δ	8.211	4.678	
$ODA_{0.50}$	β (°)	0.293	0.320	61.81
	D (nm)	27.32	25.70	
	Strain	1.340	1.514	
	Dislocation	9.860	5.246	
280℃				
Pristine	β (°)	0.159	0.227	73.94
	D (nm)	50.37	36.21	
	Strain	0.394	0.763	
	Dislocation	5.340	3.730	
$ODA_{0.15}$	β (°)	0.153	0.204	75.27
	D (nm)	51.50	37.63	
	Strain	0.377	0.706	
	Dislocation	5.168	3.370	
$0DA_{0.25}$	β (°)	0.214	0253	72.66
	D (nm)	78.21	51.21	
	Strain	0.164	0.381	
	Dislocation	7.224	4.173	

crystallite size for $ODA_{0.25}$ and $ODA_{0.50}$ films. A similar trend is evident in the (200) plane (Fig. 3d), where peak broadening and asymmetry intensify with higher ODAI incorporation. The (100) and (200) planes also revealed reduced micro strain and dislocation density in the $ODA_{0.15}$ film as observed in the inset Fig. 3c and inset Fig. 3d. Furthermore, the absence of decomposition products upon annealing at 240 °C suggests that partial substitution with ODAI is structurally viable. This strategy may be advantageous for tuning surface and interfacial properties in device architectures, albeit with a trade-off in crystallinity.

The films annealed at 280℃ also revealed strong diffraction peaks at 2θ: 14.7° and 29.8° confirming the preservation of $CsPbI_2Br$ perovskite phase except in $ODA_{0.50}$ composition as shown in Fig. 4a. The $ODA_{0.25}$ and $ODA_{0.50}$ films show additional low angle peaks at 11.19° typically associated with quasi-2D layered perovskite phases [17]. These features are indicative of the formation of Ruddlesden-Popper-like structures or low-dimensional phases due to the templating effect of the bulky ODA^+. The gradual suppression of the dominant 3D perovskite peaks shown in Fig. 4a and the emergence of layered phase features suggest a transition from a pure 3D perovskite structure (pristine and low-ODA incorporated films) to a mixed 2D/3D or quasi-2D structure at higher ODA-concentrations. These findings demonstrate that ODA^+ incorporation can effectively modulate the dimensionality and structural characteristics of $CsPbI_2Br$ perovskite. The introduction of long chain alkylammonium species disrupts the

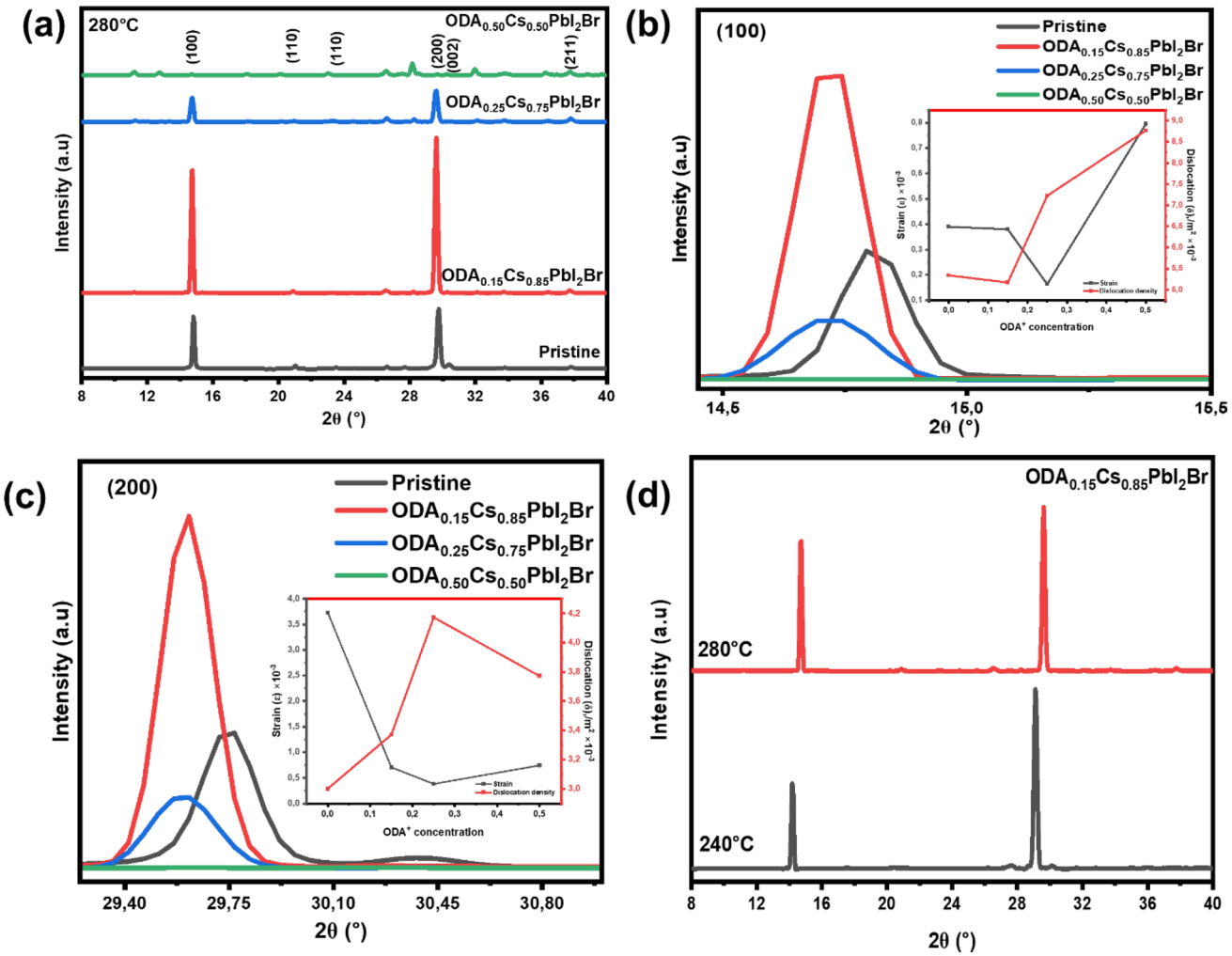

Figure 4 **a** XRD of ODA_x $Cs_{1-x}PbI_2Br$ films annealed at 280 ℃, **b** Zoomed-in view of (100) reflection with strain and dislocation data (inset), **c** Zoomed-in view (200) reflection with strain and dislocation data (inset), **d** XRD of $ODA_{0.15}$ at 240 and 280 ℃.

continuous 3D network, particularly at higher concentrations, potentially enhancing moisture resistance while modifying charge transport behaviour.

Peak broadening and a reduction in intensity can be observed in $ODA_{0.25}$ followed by a complete phase change and perovskite suppression for $ODA_{0.50}$ concentrations indicating a decrease in crystallite size and the formation of more disordered structures due to the incorporation of large ODA^+ cations. The peak at 2θ: 30.3° was suppressed and in contrast the peak at 2θ: 29.7 shifted towards lower 2θ angles suggesting an increase in lattice parameters which may correspond to the expansion of the crystal structure upon the incorporation of ODA^+. The inset in Fig. 4b evaluates the micro strain and dislocation density as function of ODA^+ incorporation in the (100) diffraction plane. Both parameters show minimum dislocation for $ODA_{0.15}$ and lowest micro strain for $0DA_{0.25}$ prior increasing to indicate the accumulation of lattice distortions and defect density introduced by the organic cation at higher concentration. The zoomed-in Fig. 4b shows high peak intensity for (100) plane in $ODA_{0.15}$ film resulting from the increase in crystallite size from 50.37 to 51.50 nm as shown in Table 2. The crystallite size was observed to also increase in the $ODA_{0.15}$ film from 36.21 to 37.63 nm in the (200) plane ultimately increasing the peak intensity as observed in Fig. 4c. High intensity of the (200) plane for $ODA_{0.15}$ may be attributed to the low dislocation density observed in the inset of Fig. 4c at an annealing temperature of 280 ℃. The lattice distortion may occur at $ODA_{0.25}$, reducing the intensity of the diffraction peak. These results suggest that stoichiometric ratio plays a pivotal role in maintaining structural purity thereby desired device functionality. A direct comparison of $ODA_{0.15}$ sample at annealed at 240 ℃ and 280 ℃ are presented in Fig. 4d revealing a slight peak shift to higher 2θ angles. The observed peak shift may result from the crystal lattice contraction at 280℃.

Morphological properties

Figure 5 presents the surface morphology of $CsPbI_2Br$ film at annealing temperatures ranging from 200–300 ℃. All the samples show compact pinhole-free morphology. At 200 ℃, the film exhibits large densely packed plate-like grains with significant surface irregularity and well-defined grain boundaries as shown in Fig. 5a. The morphology of the film annealed at 220 ℃ depicted in Fig. 5b shows a decrease in the number of grains observed and the appearance of rod-like structures. Grains with a fine texture and increased uniformity can be observed in Fig. 5c at an annealing temperature of 240 ℃. Upon increasing the temperature to 260 ℃, the film morphology in Fig. 5d shows a

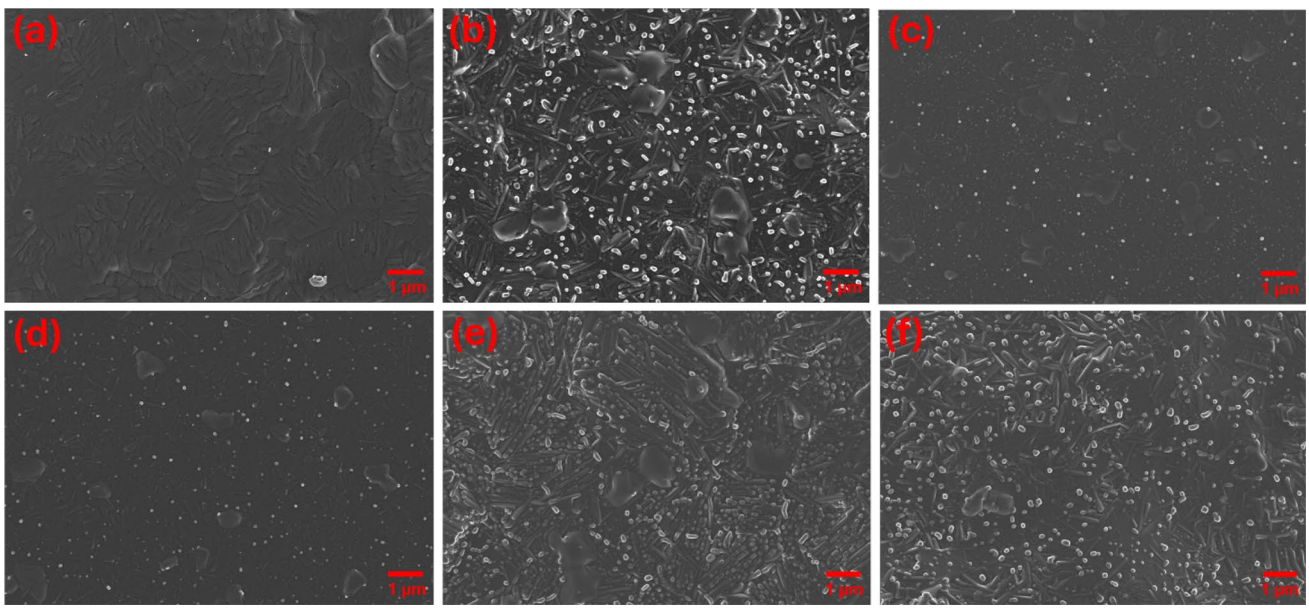

Figure 5 FE-SEM images of $CsPbI_2Br$ annealed at various temperatures of **a** 200 ℃, **b** 220 ℃, **c** 240 ℃, **d** 260 ℃, **e** 280 ℃, **f** 300 ℃.

transformation into a dense, compact microstructure with reduced porosity and improved grain connectivity, indicating enhanced crystallinity and film uniformity. Grain refinement at 280 ℃ appears to persist in Fig. 5e. The film has dense morphology with some irregularities or secondary phases emerging. In Fig. 5f, slight roughness and fragmentation at annealing temperature of 300 ℃ can be observed. The surface shows clusters or partial degradation by over-annealing, suggesting a thermal threshold beyond which the film morphology begins to deteriorate. These trends align with the XRD data, where peak sharpness and intensity increase with temperature reaching an optimum at 260–280 ℃. The sharp (200) reflection and reduced FWHM suggest significant grain growth and lattice ordering, as further supported by Sherrer-based crystallite size estimations.

The effect of ODA^+ incorporation and annealing temperature on the morphology of $CsPbI_2Br$ perovskite films was systematically investigated using FE-SEM as shown in Fig. 6. Table 3 presentsthe diameter of the grains in the FE-SEM micrographs of ODA^+-treated samples was calculate with the help of ImageJ to acquire the area of the grain and converted to the diameter using *Eq.* 3.

Table 3 Diameter of ODA^+-incorporated films representing the estimation for grain sizes of the perovskite layers

ODA^+ concentration	$ODA_{0.15}$ (240℃)	$ODA_{0.15}$ (280℃)	$ODA_{0.25}$ (240℃)	$ODA_{0.25}$ (280℃)	$ODA_{0.50}$ (240℃)
Diameter (μm)	9.005	8.849	9.099	8.858	8.684

$$Diameter = 2 \times \sqrt{\frac{Area}{2}} \tag{3}$$

A diameter of 9.005 μm for $ODA_{0.15}Cs_{0.85}PbI_2Br$ was calculated and found to be larger than that of the film annealed at higher temperature for ODA-treated films. A similar trend is observed for $ODA_{0.25}Cs_{0.75}PbI_2Br$ perovskite film. Films with low ODA^+ concentration are observed to have larger grains which decrease with increasing concentration of the organic ligand. The grain reduction with increasing concentration could result from the modification in crystal structure by the organic long chain which may facilitate fast crystallization at high temperatures.

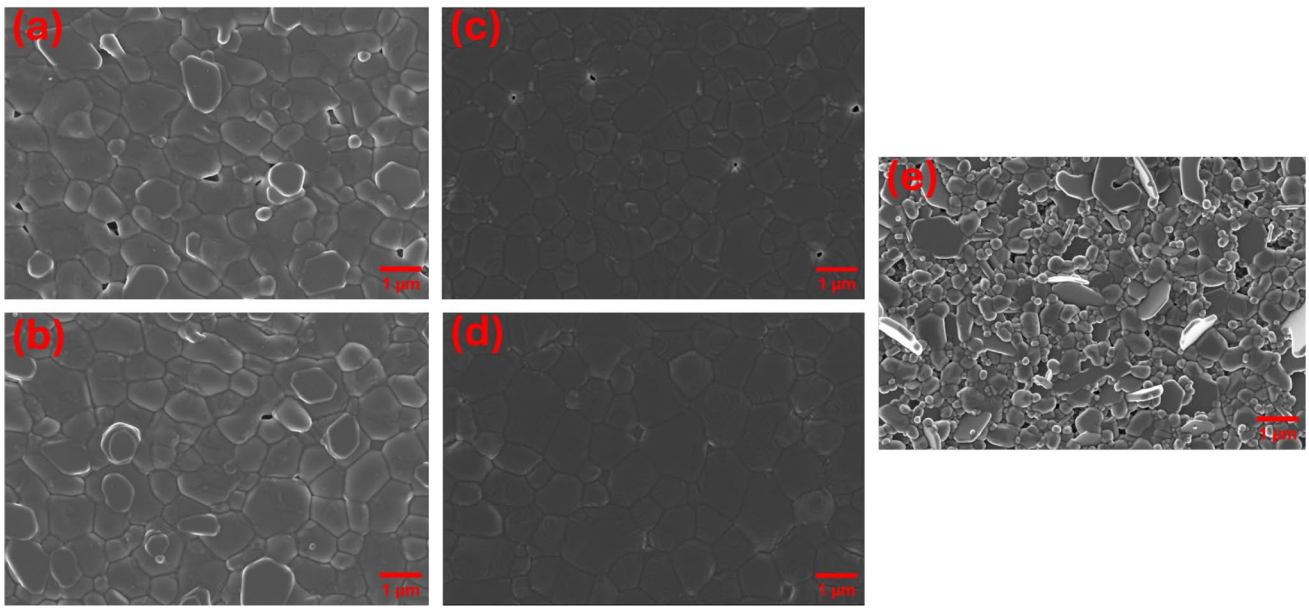

Figure 6 FE-SEM micrographs of $ODA_{0.15}Cs_{0.85}PbI_2Br$ at **a** 240 ℃, **b** 280℃. And $ODA_{0.25}Cs_{0.75}PbI_2Br$ at **c** 240℃, **d** 280 ℃. **e** $ODA_{0.50}Cs_{0.50}PbI_2Br$ at 240 ℃.

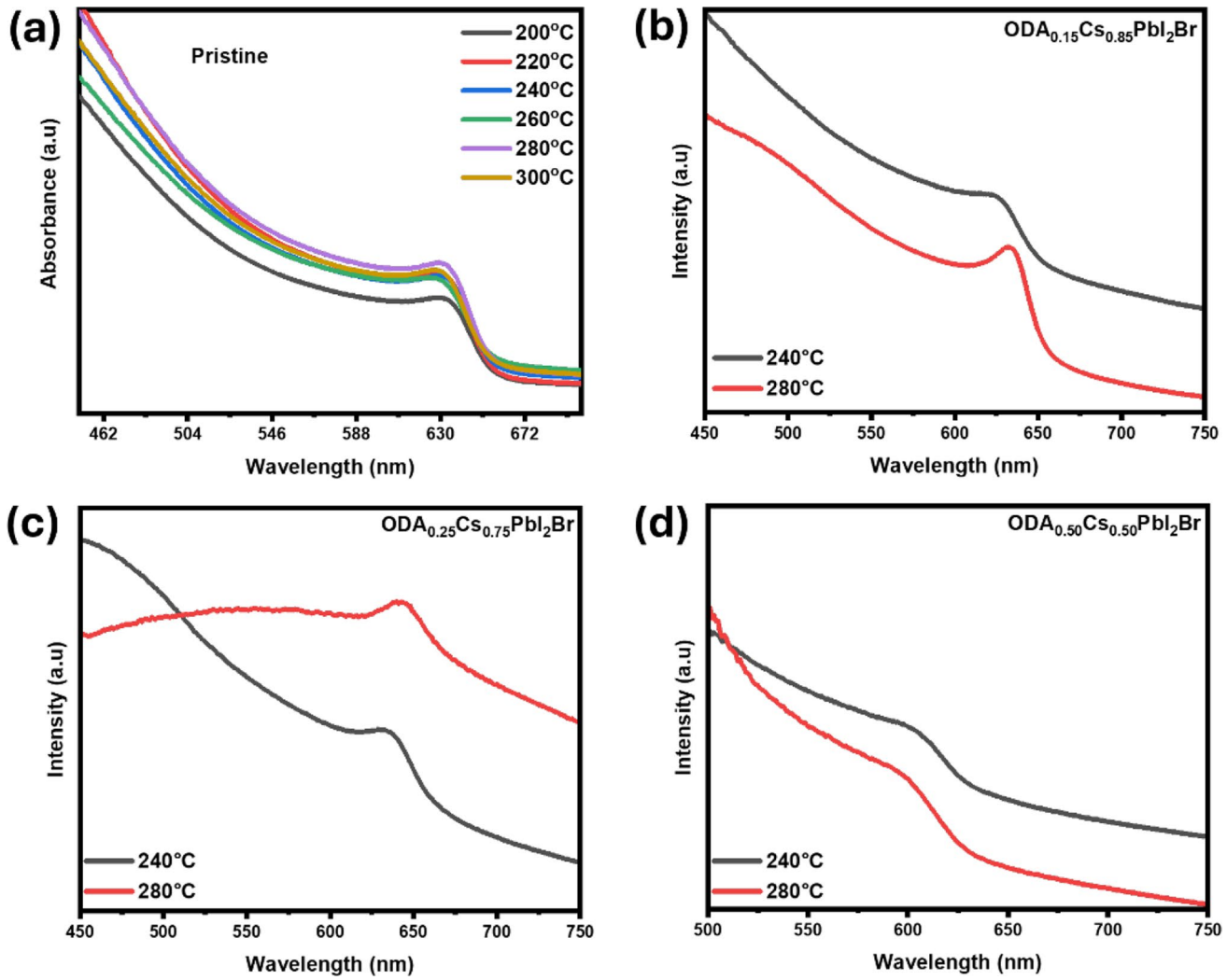

Figure 7 **a** UV–vis absorption spectra of $CsPbI_2Br$ films at different annealing temperatures, **b** $ODA_{0.15}$, **c** $ODA_{0.25}$, and **d** $ODA_{0.50}$ samples anealed at 240 and 280 ℃.

Optical properties

Figure 7 shows the optical absorption of the pristine and.

$ODA_xCs_{1-x}PbI_2Br$ perovskite thin films. The temperature-dependant absorption spectra of $CsPbI_2Br$ were measured over a range of temperatures from 200–300 ℃ as depicted in Fig. 7a. It is worth noting that no new absorption peaks appear as the temperature increases, and the bandgaps exhibit negligible variation with increasing temperature indicating the material's thermal stability. The spectrum indicates a broadband absorption band between 620 and 650 nm. Figure 7b shows the UV–vis absorption spectra of $ODA_{0.15}Cs_{0.85}PbI_2Br$ perovskite annealed at 240 and 280 ℃ to illustrate any possible shifts in optical absorption edges. A red shift in the absorption onset at high annealing temperature of 280℃ suggests narrowing of the bandgap. Perovskite films with $ODA_{0.25}$ and $ODA_{0.50}$ compositions depicted in Fig. 7c and Fig. 7d, respectively, revealed a similar trend with varying absorption intensities. This trend is attributed to the enhanced crystallinity and reduced defect density.

Figure 8 shows the absorption spectra with associated band gap estimations from Tauc's plot extraction method. A broadband absorption similar to that of the pristine film can be observed with the incorporation of the organic ligand. Figure 8a and Fig. 8b reveal that $ODA_{0.25}Cs_{0.85}PbI_2Br$ and $ODA_{0.50}Cs_{0.50}PbI_2Br$ perovskites films annealed at 240 and 280 ℃ have the

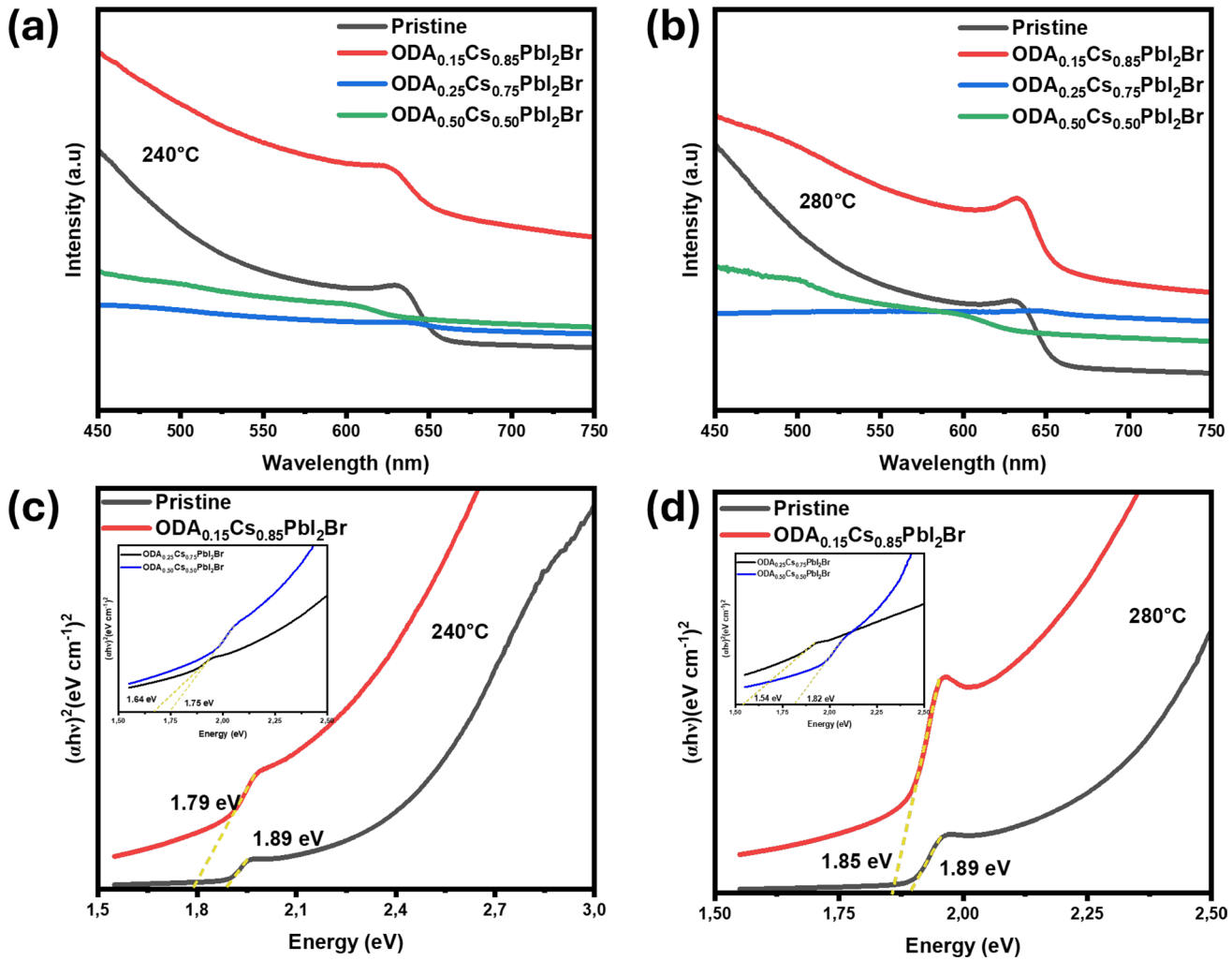

Figure 8 Absorption spectra of pristine and ODAI-substituted films at **a** 240℃, and **b** 280℃. Tauc plots $(\alpha h\nu)^2$ vs.hν used for band gap estimation at **c** 240 ℃, and **d** 280 ℃ annealing temperatures.

lowest absorption intensities and broadening of the absorption edges indicating a potential disruption of the perovskite lattice. Consistent with previous reports, an increase in absorption can be observed in $ODA_{0.15}Cs_{0.85}PbI_2Br$ perovskite film indicating successful intercalation of ODA^+ into PbX_2 structure because of strong coordination and low activation energy for interaction between ODA^+ and Pb^{2+} ions [15]. Linear extrapolation during the estimation of the bandgaps shown in Fig. 8c and Fig. 8d indicates that the bandgap slightly increases with increasing ODAI concentration, consistent with quantum confinement and structural distortion effects facilitated by the partial cation substitution.

The pristine film with a bandgap of 1.9 eV is consistent to the reported bandgaps for $CsPbI_2Br$ perovskite. Beal et al., substituted the $CsPbI_3$ with 33% Br in a solution deposition method at an annealing temperature of 315 ℃ and achieved a band gap of 1.9 eV with improved optical stability [18]. In this work, $CsPbI_2Br$ bandgap was reduced to 1.79 eV with $ODA_{0.15}Cs_{0.85}PbI_2Br$ perovskite thin film as a result of the relaxation in the lattice structure. Ibrahim et al., inferred that the synthesis of double cation perovskite is essential for engineering the band gap in perovskite materials [19]. In a study where methylammonium (MA) is partially substituted using formamidinium (FA) in $MAPbI_3$ perovskite, the bandgap can be reduced from ~ 1.52 eV to ~ 1.45 eV. This may be attributed to the larger size of the monovalent FA^+ cation [20]. The inset Fig. 8c shows an increase in bandgap for $ODA_{0.25}Cs_{0.75}PbI_2Br$ and $ODA_{0.50}Cs_{0.50}PbI_2Br$

perovskite to 1.64 eV and 1.75 eV, respectively at 240 ℃. A similar trend is observed at annealing temperature of 280℃ were the $ODA_{0.25}Cs_{0.75}PbI_2Br$ and $ODA_{0.50}Cs_{0.50}PbI_2Br$ to showed an increase in bandgap from 1.54 eV to 1.82 eV as shown in the inset Fig. 8d. This suggest that the absorption saturation is reached above $ODA_{0.25}$.

Photoluminescence (PL) spectra of $CsPbI_2Br$ and partially ODAI-substituted perovskite films are presented in Fig. 9a. The presented samples were selected to highlight the most distinct differences in PL intensities to elucidate radiative recombination with respect to ODA^+ incorporation. A relatively broad emission peak centred at ~ 650 nm with moderate PL intensity is indicative of typical emission from a polycrystalline perovskite with non-negligible defect density [21]. The emission peak position confirmed the band gap of the $CsPbI_2Br$ film observed in the UV–vis absorption spectra. It is worth noting that the PL intensity increases with 15 mol% ODA^+ concentration demonstrating successful film passivation. This is attributed to the incorporation of the long chain organic ammonium ions, which preferentially locate at grain boundaries and defects on the surface, reducing non-radiative recombination. Since PL intensity and sharp peak are highly sensitive to nonradiative recombination, these measurements provide direct insight into defect passivation and carrier dynamics. In particular, the incorporation of ODA is expected to reduce trap-assisted recombination and enhance radiative efficiency, which is reflected in stronger PL emission. Additionally, a slight redshift is observed, suggesting bandgap narrowing as shown in the optical absorption characteristics. This observation can be attributed to the enhanced crystallinity and reduced disorder within the perovskite lattice during the incorporation of moderate amounts of ODAI. In contrast, the PL intensity for the $ODA_{0.25}Cs_{0.75}PbI_2Br$ perovskite decreases with a slight blueshift consistent with bandgap measurements in Fig. 8 compared to the $ODA_{0.15}$ film. This decline may result from excess ODAI disrupting the perovskite lattice, leading to increased micro strain as shown in structural properties, which could introduce new non-radiative recombination pathways. The observed trend may reflect a change in electronic band structure due to reduced dimensionality or altered orbital overlap between Pb and halide atoms. Figure 9b shows the corresponding full width at half maximum (FWHM) values extracted from the PL spectra. The FWHM narrows with low ODAI concentration, supporting the hypothesis of improved crystal quality or defect passivation. These results indicate that moderate incorporation of ODAI (specifically at 15 mol%) is beneficial for enhancing the optoelectronic properties of $CsPbI_2Br$ films, while higher substitution concentrations may not be beneficial for the material's structural and optical properties. The enhanced PL intensity and reduced defect-mediated recombination in the $ODA_{0.15}$ film suggest its promise for improved performance in optoelectronic devices such as solar cells.

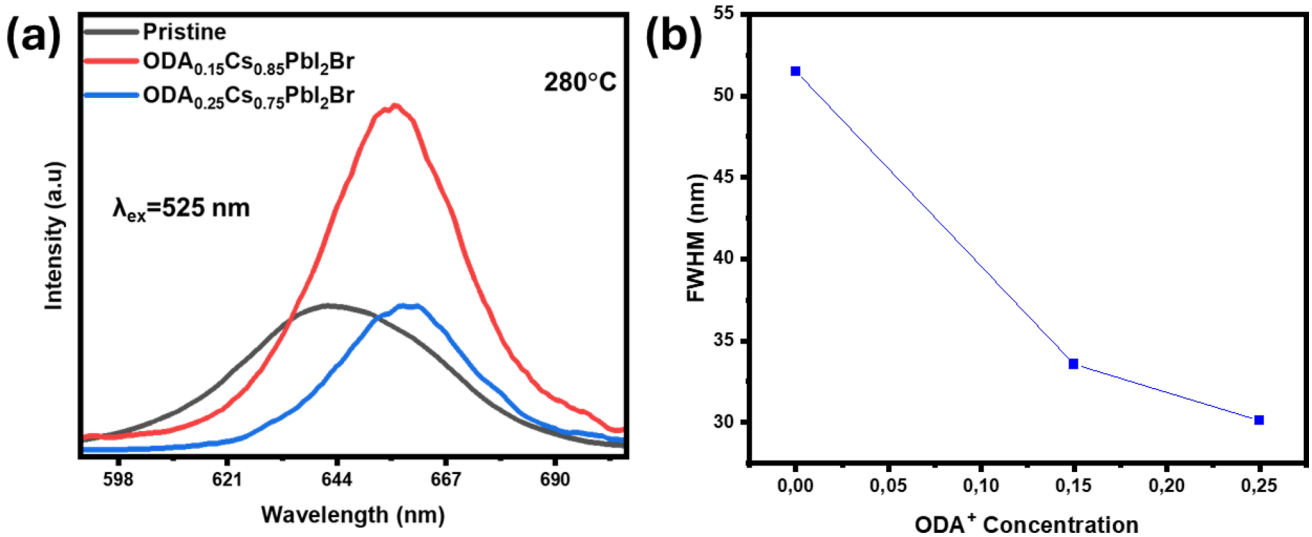

Figure 9 PL spectra of pristine and ODAI-substituted films ($ODA_{0.15}$ and $ODA_{0.25}$), **b** Extracted FWHM of PL emission peaks as a function of ODAI concentration.

Summary and conclusions

In this study, a qualitative analysis of the effects of annealing and partial substitution of Cs^+ with ODA^+ on the structural, morphological, and optoelectronic properties of $CsPbI_2Br$ perovskite thin films are present. The results revealed that the annealing temperature influences the crystallinity, defect density, and morphology of the films. XRD diffractograms confirmed a tetragonal crystal structure for $CsPbI_2Br$ perovskite and a phase transition at an annealing temperature of 280 ℃ and above. Optimal $CsPbI_2Br$ perovskite film quality was achieved between 240 and 280 ℃, with the films at 280 ℃ revealing the formation of a new $CsPbBr_3$ perovskite phase. The incorporation of a 15 mol% of ODAI effectively passivates defects, reduces micro strain and dislocation density, and enhances film uniformity without altering the 3D perovskite structure. Thermal annealing induced sharp peaks consistence with improved crystallinity. At 240 ℃ the FWHM was reduced by ~ 20% for the (100) plane and ~ 13% for the (200) plane, while at 280 ℃ the corresponding reductions were ~ 3.8% and ~ 10%, respectively. These reductions imply an increase in crystallite size which is expected to reduce grain boundary density and enhance carrier transport pathways, thereby corroborating more efficient charge extraction and improved optoelectronic performance in downstream device applications. These improvements lead to enhanced light absorption, narrowed optical bandgaps, and significantly higher photoluminescence intensity, indicating suppressed non-radiative recombination. The integration of the absorption spectra confirmed substantial enhancement with ODA^+ incorporation, where the integrated area increased from 16.7 nm (pristine) to 34.9 nm ($ODA_{0.15}$) at 240 ℃, and from 14.0 nm (pristine) to 29.0 nm ($ODA_{0.15}$), highlighting the significantly stronger light-harvesting capability of the modified films. However, excess incorporation of ODA^+ to $ODA_{0.25}$ and $ODA_{0.50}$ introduces structural disorder, reduces crystallinity, and degrades optoelectronic performance. The band gap of the pristine film remained the same as the annealing temperature was increased from 200–300 ℃. On the other hand, the incorporation of ODA^+ decreased the band gap of the pristine film. The optical band gap narrowed with ODA^+ incorporation, decreasing by ~ 5.3% at 240 ℃ and ~ 2.1% at 280 ℃ relative to the pristine films, thereby extending absorption toward longer wavelengths and enhancing solar spectrum utilization. These quantified improvements are expected to reduce defect density, improve carrier transport, and support ~ 15–20% gains in device efficiency, which can translate into lower cost-per watt and improved economic viability of perovskite optoelectronic devices. The results demonstrate that an approach which involves a controlled ODAI substitution and precise annealing optimization can significantly improve the performance of $CsPbI_2Br$ perovskite films.

Acknowledgements

The authors wish to thank the University of Pretoria (UP), Department of Physics, Department of Chemistry, and financial support from the National Research Foundation (SARCHI UID 115463 NRF/DSI).

Funding

Open access funding provided by University of Pretoria. National Research Foundation, U115463, Mmantsae Diale

Data availability

The data that support the findings of this study are available from the corresponding author upon reasonable request.

Declarations

Conflict of interest The authors declare no conflict of interest.

References

[1] Yang K et al (2025) First-principles studies on the structural, electronic elastic and optical properties of $CsPbI_2Br$ under pressure. Phys Scr 100(5):055966

[2] Wang Z et al (2020) Over 1 μm electron-hole diffusion lengths in $CsPbI_2Br$ for high efficient solar cells. J Power Sources 454:227913

[3] Sutton RJ et al (2016) Bandgap-tunable cesium lead halide perovskites with high thermal stability for efficient solar cells. Adv Energy Mater 6(8):1502458

[4] Ustinova MI et al (2025) Towards stable wide-bandgap perovskite absorbers: controlling light-induced halide phase segregation in $CsPbI_2Br$ through partial lead substitution. Mendeleev Commun 35(5):573–576

[5] Pan J et al (2021) Morphology control of perovskite film for efficient $CsPbIBr_2$based inorganic perovskite solar cells. Sol Energy Mater Sol Cells 221:110878

[6] Zheng K et al (2021) Improved phase stability of $CsPbI_2Br$ perovskite by released microstrain toward highly efficient and stable solar cells. InfoMat 3(12):1431–1444

[7] Tara A et al (2022) Theoretical optimization of defect density and band offsets for $CsPbI_2Br$ based perovskite solar cells. Mater Today Commun 33:104546

[8] Chen S-C, Wang D, Zheng Q (2020) Surface passivation of all-inorganic $CsPbI_2Br$ with a fluorinated organic ammonium salt for perovskite solar cells with efficiencies over 16%. Solar RRL 4(10):2000321

[9] Fan Y et al (2019) Scalable ambient fabrication of high-performance $CsPbI_2Br$ solar cells. Joule 3(10):2485–2502

[10] Ozturk T et al (2021) Composition engineering of operationally stable $CsPbI_2Br$ perovskite solar cells with a record efficiency over 17%. Nano Energy 87:106157

[11] Yu F et al (2023) High-quality all-inorganic $CsPbI_2Br$ thin films derived from phase-pure intermediate for efficient wide-bandgap perovskite solar cells. J Solid State Chem 317:123728

[12] Wu C et al (2020) A study on the effects of mixed organic cations on the structure and properties in lead halide perovskites. Phys Chem Chem Phys 22(5):3105–3111

[13] Kong X et al (2019) Complete suppression of detrimental polymorph transitions in all-inorganic perovskites via nanoconfinement. ACS Appl Energy Mater 2(4):2948–2955

[14] Nam JK et al (2017) Unveiling the crystal formation of cesium lead mixed-halide perovskites for efficient and stable solar cells. J phys chem lett 8(13):2936–2940

[15] Duan Z et al (2021) Highly luminescent and stable 2d/3d octadecylammonium/formamidinium lead bromide perovskite films. J Phys Chem C 125(31):17501–17508

[16] Wang A et al (2022) Inhibiting octahedral tilting for stable $CsPbI_2Br$ solar cells. InfoMat 4(1):e12263

[17] Leung TL et al (2022) Stability of 2D and quasi-2D perovskite materials and devices. Commun Mater 3(1):63

[18] Beal RE et al (2016) Cesium lead halide perovskites with improved stability for tandem solar cells. J Phys chem lett 7(5):746–751

[19] Ibrahim et al (2024) Emerging trends in low band gap perovskite solar cells: materials device architectures and performance optimization. Molecular Phys 122(17):e2316273

[20] Amat A et al (2014) Cation-induced band-gap tuning in organohalide perovskites: interplay of spin–orbit coupling and octahedra tilting. Nano Lett 14(6):3608–3616

[21] Xu J et al (2022) Stable high-efficiency $CsPbI_2Br$ solar cells by designed passivation using multifunctional 2D perovskite. Adv Func Mater 32(33):2202829